











RESEARCH ARTICLE

Magnetic Resonance in Medicine

QRAGE—Simultaneous multiparametric quantitative MRI of water content, T_1 , T_2^* , and magnetic susceptibility at ultrahigh field strength

Markus Zimmermann¹  | Zaheer Abbas¹  | Yannic Sommer¹  |
 Alexander Lewin²  | Shukti Ramkiran^{1,3}  | Jörg Felder^{1,4}  |
 Wieland A. Worthoff¹  | Ana-Maria Oros-Peusquens¹  | Seong Dae Yun¹  |
 N. Jon Shah^{1,2,5,6} 

¹Forschungszentrum Jülich, Institute of Neuroscience and Medicine–4, Jülich, Germany

²Forschungszentrum Jülich, Institute of Neuroscience and Medicine–11, Jülich, Germany

³Department of Psychiatry, Psychotherapy and Psychosomatics, RWTH Aachen University, Aachen, Germany

⁴RWTH Aachen University, Aachen, Germany

⁵JARA–BRAIN–Translational Medicine, Aachen, Germany

⁶Department of Neurology, RWTH Aachen University, Aachen, Germany

Correspondence

Markus Zimmermann,
 Forschungszentrum Jülich, Jülich 52425,
 Germany.
 Email: m.zimmermann@fz-juelich.de

Funding information

Deutsche Forschungsgemeinschaft,
 Grant/Award Number: 446320670

Abstract

Purpose: To introduce quantitative rapid gradient-echo (QRAGE), a novel approach for the simultaneous mapping of multiple quantitative MRI parameters, including water content, T_1 , T_2^* , and magnetic susceptibility at ultrahigh field strength.

Methods: QRAGE leverages a newly developed multi-echo MPnRAGE sequence, facilitating the acquisition of 171 distinct contrast images across a range of TI and TE points. To maintain a short acquisition time, we introduce MIRAGE2, a novel model-based reconstruction method that exploits prior knowledge of temporal signal evolution, represented as damped complex exponentials. MIRAGE2 minimizes local Block-Hankel and Casorati matrices. Parameter maps are derived from the reconstructed contrast images through postprocessing steps. We validate QRAGE through extensive simulations, phantom studies, and in vivo experiments, demonstrating its capability for high-precision imaging.

Results: In vivo brain measurements show the promising performance of QRAGE, with test–retest SDs and deviations from reference methods of < 0.8% for water content, < 17 ms for T_1 , and < 0.7 ms for T_2^* . QRAGE achieves whole-brain coverage at a 1-mm isotropic resolution in just 7 min and 15 s, comparable to the acquisition time of an MP2RAGE scan. In addition, QRAGE generates a contrast image akin to the UNI image produced by MP2RAGE.

Conclusion: QRAGE is a new, successful approach for simultaneously mapping multiple MR parameters at ultrahigh field.

KEYWORDS

magnetization-prepared multi-echo gradient-echo, model-based iterative reconstruction, quantitative MRI, simultaneous multiparameter mapping, structured low-rank matrix, ultrahigh field strength

[Correction appended on 26th September 2024 after online publication: corrections to equation 9 line breaks have been updated as well as grammatical errors throughout the article.]

This is an open access article under the terms of the [Creative Commons Attribution](https://creativecommons.org/licenses/by/4.0/) License, which permits use, distribution and reproduction in any medium, provided the original work is properly cited.

© 2024 The Author(s). *Magnetic Resonance in Medicine* published by Wiley Periodicals LLC on behalf of International Society for Magnetic Resonance in Medicine.

1 | INTRODUCTION

Quantitative MRI (qMRI) has emerged as a powerful tool for measuring physiological MR parameters, offering advantages over conventional qualitative MRI in terms of sensitivity and comparability.¹ It enables the inference of specific tissue properties, which have the potential to provide deeper insights into disease pathophysiology and, consequently, the development of better therapeutic strategies. Regarding brain tissue, a few key measurable properties are water content, iron content, and myelination. These properties have been implicated in conditions such as multiple sclerosis, epilepsy, tumors, stroke, and traumatic brain injury, highlighting their importance and potential in therapeutic development.^{2–4} The quantitative parameters derivable from MRI, such as the longitudinal relaxation time T_1 , the effective transverse relaxation time T_2^* , the magnetic susceptibility of tissue, and the proton density, are directly related to these properties and provide information about them. In particular, myelination and iron content affect T_1 , T_2^* , and the magnetic susceptibility of tissue,^{5–7} and proton density reflects the percent of observed water protons in each voxel.⁸

The increasing availability of commercial 7T MRI scanners has enabled imaging with increased SNR and higher resolution, albeit with its own set of challenges. For instance, with increasing field strengths, T_1 lengthens while T_2^* shortens; the static magnetic field, B_0 , and the transmit field, B_1^+ , become more inhomogeneous; and the specific absorption rate (SAR) increases superlinearly.⁴ Thus, to leverage the full potential of ultrahigh field strength (UHF) in qMRI, there is a critical need for fast, accurate, and robust qMRI methods that are well adapted to UHF and optimized to overcome the aforementioned challenges.

In this study, we present an efficient qMRI technique, termed quantitative rapid gradient echo (QRAGE), which is tailored to application at UHF for simultaneous quantification of the four MR parameters introduced previously, namely, free water content (C_W), T_1 , T_2^* , and magnetic susceptibility (χ).

To the best of our knowledge, this study is the first to develop a method that allows the simultaneous acquisition of the four parameters at UHF strength within a relatively short acquisition time. Although several methods for the estimation of these parameters exist, they either target individual parameters or are optimized to work at lower field strengths. For instance, the variable flip angle (VFA) method, which relies on multi-echo gradient-echo (MEGE) sequences acquired at different flip angles, is used commonly for estimating C_W .^{9–12} However, a fundamental challenge of the VFA method is the impact of transmit field inhomogeneities at UHF, leading to a potential bias

in parametric estimates.¹³ It also suffers from long acquisition times and is highly susceptible to motion artifacts. Several newer methods have been developed to enable fast imaging and improved motion robustness at field strengths of up to 3 T, such as magnetic resonance fingerprinting (MRF),¹⁴ echo-planar time-resolved imaging,^{15,16} and 3D quantification using an interleaved Look-Locker acquisition sequence,^{17,18} but translation to 7 T has been challenging. The existing MRF framework, for instance, encounters issues related to high SAR and biased estimates due to B_1^+ inhomogeneities, which become particularly relevant at UHF. Although there is ongoing research dedicated to low SAR MRF sequence development¹⁹ and the incorporation of B_1^+ in the MRF dictionary,^{20,21} success at 7 T is currently limited.

A successful multiparametric qMRI approach at UHF is the multi-echo (ME) MPRAGE sequence with two TIs (ME-MP2RAGE), which extends the capabilities of the MP2RAGE sequence.^{2,22,23} This method acquires multiple gradient echoes at two inversion time points, enabling the extraction of information about T_1 , T_2^* , and χ . The ME-MP2RAGE sequence demonstrates robustness against static magnetic field and transmit field inhomogeneities, while also imposing a low SAR burden, making it well-suited for UHF applications. However, given that the Look-Locker signal adheres to a three-parameter model, the estimation of T_1 from only two inversion time points is a challenging task. In particular, it has been shown that MP2RAGE-like sequences tend to underestimate T_1 values, which is an inherent limitation associated with this approach.^{13,24} To overcome this limitation, the multi-echo magnetization-prepared rapid gradient-echo sequence with many inversion times (ME-MPnRAGE) combines a high number of sampled inversion time points with a highly accelerated acquisition and radial view-sharing to maintain a reasonable acquisition time.¹³

Although radial view-sharing, as used in the MPnRAGE sequence, has been applied successfully in inversion recovery (IR) and functional MRI sequences, its application for multi-echo spin echo (MESE) and MEGE sequences is less suitable, and model-based reconstruction techniques are preferred instead.^{25–28} Low-rank methods based on local Casorati matrices have been used to exploit correlations between voxel time series in a local neighborhood and have been applied successfully to IR and MESE data but are ineffective for MEGE data due to the influence of B_0 inhomogeneity.²⁹ Structured low-rank methods based on Hankel matrices have demonstrated their ability to address the challenges of MEGE data, exemplified by the MIRAGE method,²⁶ and have also been applied successfully to IR, MESE, and diffusion data.^{30,31}

Here, we propose QRAGE as a novel qMRI technique, comprising an imaging sequence, ME-MPnRAGE,

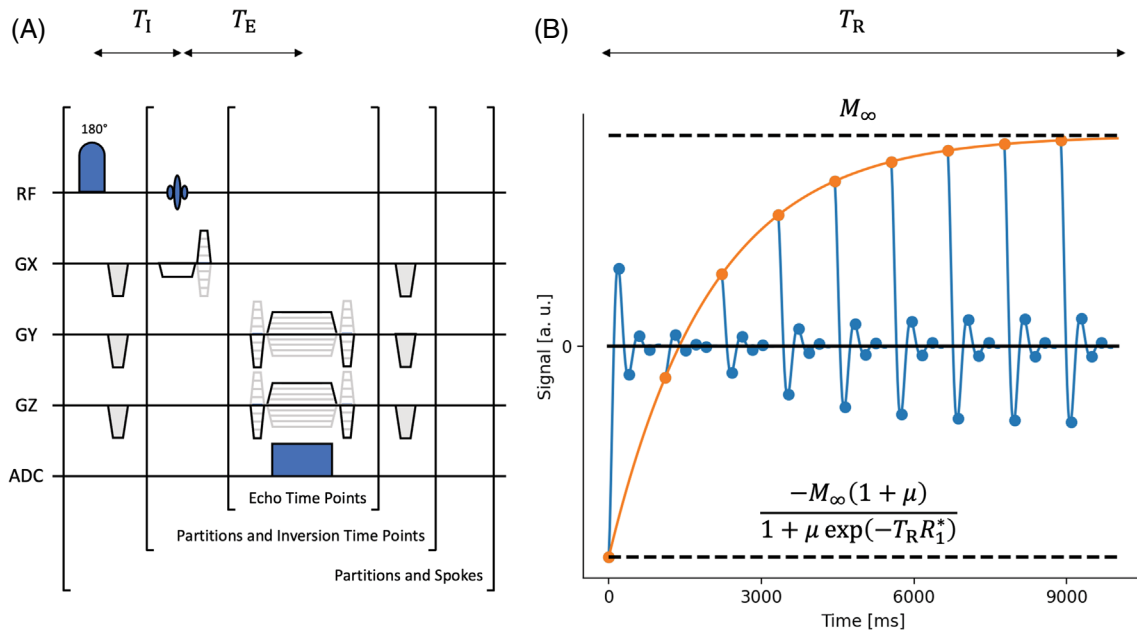


FIGURE 1 (A) Sequence diagram of the quantitative rapid gradient-echo sequence illustrating the timing and sequence of events, with the T_I and T_E . (B) Signal evolution of a single homogeneous voxel showing the inversion recovery and multi-echo gradient-echo behavior, with the T_R , the steady-state magnetization M_∞ , the effective longitudinal relaxation R_1^* , and the inversion efficiency μ .

at many T_I s, and a reconstruction technique, model-based iterative reconstruction for accelerated gradient-echo imaging with two temporal dimensions (MIRAGE2). The ME-MPnRAGE sequence builds on an extended and highly accelerated ME-MP2RAGE sequence by incorporating the acquisition of multiple T_I s and T_E s, allowing for a more comprehensive characterization of the signal evolution at each voxel. Sampling the IR curve sufficiently long also allows for the CSF magnetization to closely approach the steady state, which is essential for C_W mapping, as CSF serves as the normalization reference for 100% water content. To address the challenge of the resulting long acquisition times, we further propose a novel model-based reconstruction method, MIRAGE2, which jointly reconstructs the k-space data acquired at all time points while leveraging prior information about the spatiotemporal signal evolution of the ME-MPnRAGE sequence. Although various model-based reconstruction techniques have been developed for IR and MEGE sequences, none have been specifically tailored for the unique characteristics of the ME-MPnRAGE sequence, which combines both IR and MEGE behavior.^{26,32–34} The MIRAGE2 method builds on the MIRAGE algorithm by incorporating prior knowledge of the temporal signal evolution through minimization of the rank of local Block-Hankel and Casorati matrices, leveraging the 2D nature of the exponentials in the sequence and exploiting their local correlations.

2 | THEORY

2.1 | Sequence and signal model

In this section, we provide a comprehensive description of the proposed ME-MPnRAGE sequence. The ME-MPnRAGE sequence begins with an adiabatic inversion pulse, followed by a series of RF pulses and gradient-echo acquisitions after each RF pulse. The sequence diagram of the ME-MPnRAGE sequence is shown in Figure 1A. This multi-echo, Look-Locker-based sequence enables the independent capture of longitudinal and transverse relaxation dynamics. We assume that, in a general multi-echo Look-Locker-based sequence, the time signal $\mathbf{X}(\mathbf{r}) \in \mathbb{C}^{N_I \times N_E}$ of each voxel at position \mathbf{r} with the number of sampled inversion time (T_I) and echo time (T_E) points N_I and N_E can be represented as a summation of 2D damped complex exponentials, as follows:

$$x_{m,n}(\mathbf{r}) = \sum_{q=1}^{N_Q(\mathbf{r})} M_{\infty,q}(\mathbf{r}) \left[1 - \frac{(1 + \mu(\mathbf{r})) \exp(-T_{I,m} R_{1,q}^*(\mathbf{r}))}{1 + \mu(\mathbf{r}) \exp(-T_R R_{1,q}^*(\mathbf{r}))} \right] \exp(-T_{E,n} (R_{2,q}^*(\mathbf{r}) + i\omega_q(\mathbf{r}))), \quad (1)$$

where $N_Q(\mathbf{r})$ is the number of tissue compartments; $m \in [1, N_I]$, $n \in [1, N_E]$, and $q = [1, N_Q(\mathbf{r})]$ are the T_I , T_E , and compartment indices, respectively; M_∞ is the steady-state

magnetization; R_1^* and R_2^* are the effective longitudinal and transverse relaxation rates, respectively; ω is the local resonance frequency; and μ is the inversion efficiency. A representative signal evolution of a single voxel is depicted in Figure B.

These parameters are interconnected with the equilibrium longitudinal magnetization M_0 and the longitudinal relaxation rate R_1 through the following relationships:

$$M_0(\mathbf{r}) = \frac{M_{\infty,q}(\mathbf{r})}{\sin(\alpha(\mathbf{r}))} \frac{1 - \cos(\alpha(\mathbf{r})) \exp(-T_\alpha R_1(\mathbf{r}))}{1 - \exp(-T_\alpha R_1(\mathbf{r}))} \quad (2a)$$

$$R_1(\mathbf{r}) = R_1^*(\mathbf{r}) - \frac{\log(\cos(\alpha(\mathbf{r})))}{T_\alpha}, \quad (2b)$$

where α is the apparent flip angle, and T_α is the time between two RF pulses. The equilibrium longitudinal magnetization is directly proportional to the concentration of free water, C_w , and the magnetic susceptibility of tissue, χ , is linked to the local resonance frequency through spatial dipole convolution.^{35–37} Additionally, the longitudinal relaxation time is given by $T_1 = 1/R_1$, while the effective transverse relaxation time is expressed as $T_2^* = 1/R_2^*$.

2.2 | Model-based reconstruction

Here, we introduce the concept of low-rank Hankel and Casorati matrices to model the signal behavior and describe the proposed reconstruction method, MIRAGE2. At each voxel position \mathbf{r} , one can form local Block-Hankel matrices as follows:

$$\mathbf{B}(\mathbf{r}) = \begin{bmatrix} \mathbf{H}_1(\mathbf{r}) & \cdots & \mathbf{H}_{\Gamma_1}(\mathbf{r}) \\ \vdots & \ddots & \vdots \\ \mathbf{H}_{\Gamma_1}(\mathbf{r}) & \cdots & \mathbf{H}_{N_l}(\mathbf{r}) \end{bmatrix} \quad (3)$$

$$\mathbf{H}_m(\mathbf{r}) = \begin{bmatrix} x_{m,1}(\mathbf{r}) & \cdots & x_{m,\Gamma_2}(\mathbf{r}) \\ \vdots & \ddots & \vdots \\ x_{m,\Gamma_2}(\mathbf{r}) & \cdots & x_{m,N_E}(\mathbf{r}) \end{bmatrix}$$

with $\Gamma_1 = \left\lfloor \frac{N_l+1}{2} \right\rfloor$ and $\Gamma_2 = \left\lfloor \frac{N_E+1}{2} \right\rfloor$. The rank of such a Hankel matrix is bound by

$$\text{rank}(\mathbf{B}(\mathbf{r})) \leq \min\left(2 \times N_Q(\mathbf{r}), \left\lfloor \frac{N_l+1}{2} \times \frac{N_E+1}{2} \right\rfloor\right) \quad (4)$$

In particular, the rank is not higher than twice the number of tissue compartments inside the voxel and can be lower if compartments share the same effective transverse relaxation rate.

Additionally, at each voxel position \mathbf{r} , one can form local Casorati matrices as follows:

$$\mathbf{C}(\mathbf{r}) = [\mathbf{X}(\mathbf{r} + \mathbf{n}_1) \cdots \mathbf{X}(\mathbf{r} + \mathbf{n}_{N_L})], \quad (5)$$

where \mathbf{n}_l is the local neighborhood; l is the voxel index within the neighborhood; and N_L is the number of voxels in the local neighborhood. The rank of such a Casorati matrix is bound by

$$\text{rank}(\mathbf{C}(\mathbf{r})) \leq \min\left(\sum_{l=1}^{N_L} N_Q(\mathbf{r} + \mathbf{n}_l), N_l, N_E \times N_L\right) \quad (6)$$

It is not higher than the total number of compartments inside the voxels within the local neighborhood and can be lower if there are compartments that share the same effective longitudinal relaxation rate. Figure 2 illustrates the connection among the contrast images, the local neighborhood, and the constructed Hankel and Casorati matrices.

MIRAGE2 aims to reconstruct the images \mathbf{x} from the k-space data \mathbf{d} acquired at multiple TIs and TEs with respect to the temporal signal model by solving

$$\min_{\mathbf{x}} \frac{1}{2} \|\mathbf{A}\mathbf{x} - \mathbf{d}\|_2^2 + \lambda_w \|\mathbf{T}_w \mathbf{x}\|_{1,2} + \lambda_H \|\mathbf{T}_H \mathbf{x}\|_{*,1} + \lambda_C \|\mathbf{T}_C \mathbf{x}\|_{*,1}, \quad (7)$$

where \mathbf{A} is the encoding operator; \mathbf{T}_w is the wavelet operator; \mathbf{T}_H is the Hankel operator; \mathbf{T}_C is the Casorati operator; and λ_w , λ_H , and λ_C are the regularization weights. Here, the wavelet operator applies a stationary wavelet transform to each contrast image individually; the Hankel operator constructs a Block-Hankel matrix at each voxel position individually; and the Casorati operator forms a Casorati matrix at each voxel position and its local neighborhood. The mixed norm $\|\cdot\|_{1,2}$ is used as a convex surrogate for sparsity of the wavelet term using joint information between contrast images, whereas the mixed norm $\|\cdot\|_{*,1}$ acts as a convex surrogate for the rank, summing the nuclear norm over all voxel positions and local neighborhoods, respectively.

An approach similar to the MIRAGE algorithm was used to solve Eq. (7) by replacing it with an augmented Lagrangian, as follows:

$$\mathcal{L}(\mathbf{x}, \mathbf{z}, \mathbf{u}) = \lambda_w \|\mathbf{x}_w\|_{1,2} + \lambda_H \|\mathbf{x}_H\|_{*,1} + \lambda_C \|\mathbf{x}_C\|_{*,1} + \frac{\rho}{2} \left\| -\begin{pmatrix} 0 \\ \mathbf{x} \end{pmatrix} + \begin{pmatrix} \mathbf{A} \\ \mathbf{T} \end{pmatrix} \mathbf{z} + \begin{pmatrix} \mathbf{d} \\ \mathbf{u} \end{pmatrix} \right\|_2^2, \quad (8)$$

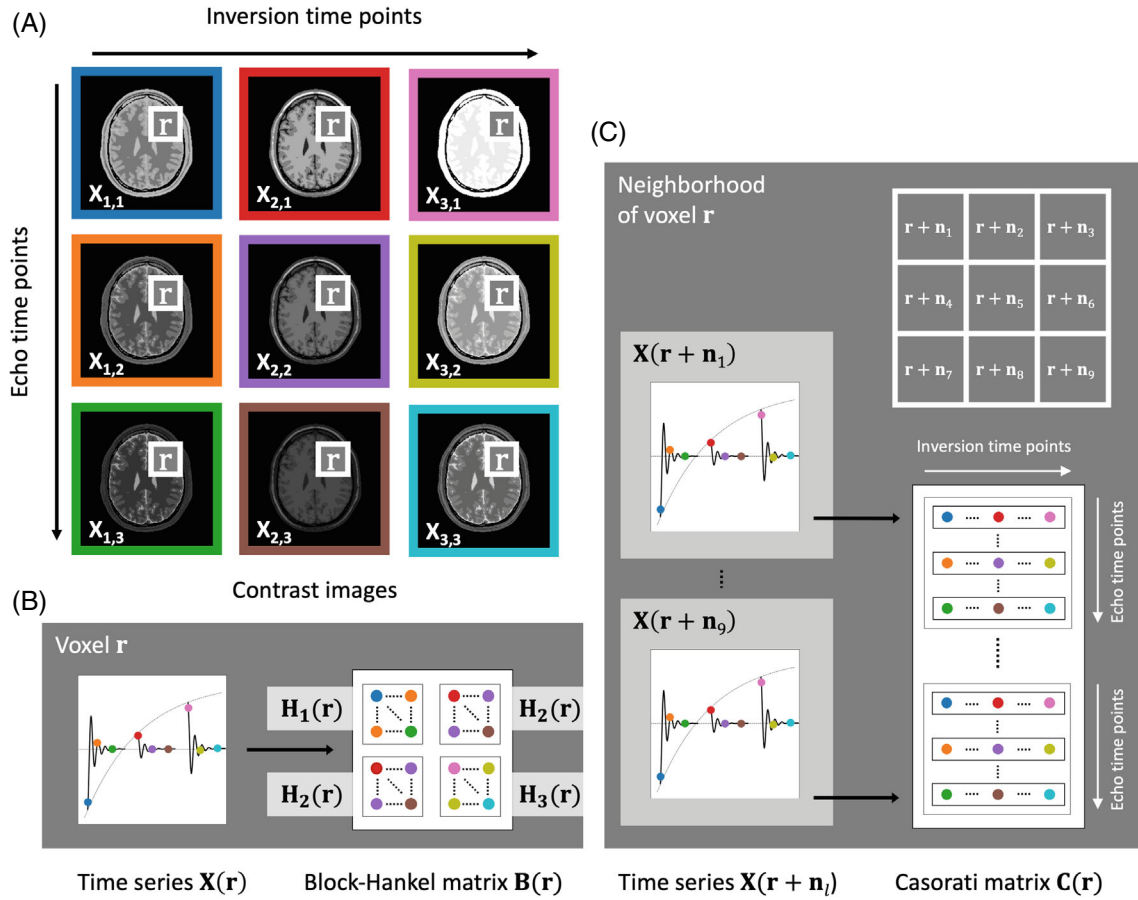


FIGURE 2 (A) Contrast images at different TIs and TEs, with a highlighted local neighborhood consistently marked in each image. (B) Voxel time series from a single voxel and the formation of the corresponding local Block-Hankel matrix. (C) Voxel time series of two example voxels from a local neighborhood and the formation of the corresponding local Casorati matrix. The time points $x_{m,n}$ are color-coded in the border color of the contrast images in (A) and the dot color in (B) and (C).

where \mathbf{z} is the primal variable; $\mathbf{x} = (\mathbf{x}_W; \mathbf{x}_H; \mathbf{x}_C)$ is the dual variable; $\mathbf{u} = (\mathbf{u}_W; \mathbf{u}_H; \mathbf{u}_C)$ is the Lagrangian multiplier; $\mathbf{T} = (\mathbf{T}_W; \mathbf{T}_H; \mathbf{T}_C)$ is the transform operator; and ρ is the penalty parameter. The alternating direction method of multipliers solves Eq. (8) by performing the following updates in an alternating fashion:

$$\begin{aligned}
 \mathbf{x}_W^{(k+1)} &= S_{\lambda_W/\rho}(\mathbf{T}_W \mathbf{z}^{(k)} + \mathbf{u}_W^{(k)}) \\
 \mathbf{x}_H^{(k+1)} &= \mathcal{V}_{\lambda_H/\rho}(\mathbf{T}_H \mathbf{z}^{(k)} + \mathbf{u}_H^{(k)}) \\
 \mathbf{x}_C^{(k+1)} &= \mathcal{V}_{\lambda_C/\rho}(\mathbf{T}_C \mathbf{z}^{(k)} + \mathbf{u}_C^{(k)}) \\
 \mathbf{z}^{(k+1)} &= (\mathbf{A}^T \mathbf{A} + \mathbf{T}^T \mathbf{T})^{-1} (\mathbf{A}^T \mathbf{d} + \mathbf{T}^T (\mathbf{x}^{(k+1)} - \mathbf{u}^{(k)})) \\
 \mathbf{u}^{(k+1)} &= \mathbf{u}^{(k)} - \mathbf{x}^{(k+1)} + \mathbf{T} \mathbf{z}^{(k+1)},
 \end{aligned} \quad (9)$$

where k is the iteration index; $S_\lambda(\mathbf{x})$ is the soft-thresholding operator; and $\mathcal{V}_\lambda(\mathbf{x})$ is the singular-value soft-thresholding operator until a suitable stopping criterion is reached. The \mathbf{x} and \mathbf{u} updates have analytic solutions and can be executed in parallel. The \mathbf{z} update is carried out by solving the conjugate gradient algorithm on the normal equation

and can be performed efficiently via Toeplitz embedding of $\mathbf{A}^T \mathbf{A}$ exploiting $\mathbf{T}^T \mathbf{T} = \mathbf{T}_W^T \mathbf{T}_W + \mathbf{T}_H^T \mathbf{T}_H + \mathbf{T}_C^T \mathbf{T}_C$ being diagonal.

3 | METHODS

3.1 | Data acquisition

A stack-of-stars trajectory was used in this study, consisting of a golden-angle radial sampling trajectory³⁸ and a segmented MPRAGE-like readout,³⁹ acquiring 16 partitions after each adiabatic inversion pulse (see Figure S1). The radial sampling pattern offers spatial and temporal incoherence, meaning that it samples different parts of k-space at each TI and TE and is highly robust to motion. Moreover, the sequence can be terminated at any time without compromising the usability of the acquired data, although image resolution and SNR may be affected. The experiments in this study aimed to assess the accuracy and reliability of QRAGE. To address the former, reference

methods, used widely as gold standards, were acquired for each quantitative parameter. For the latter, longitudinal test–retest experiments were performed.

All experiments were performed using a commercial 7T scanner (MAGNETOM Terra; Siemens Healthineers, Erlangen, Germany). A 32-element head coil (Nova Medical Head Coil 1TX/32RX; Nova Medical, MA, USA) was used for excitation and signal reception in both phantom and in vivo experiments.

The imaging protocol included a stack-of-stars ME-MPnRAGE sequence, using the radial sampling pattern described previously. Each partition used the same k-space undersampling pattern. The sequence parameters were as follows: $T_R = 9055$ ms, $T_{E,1} = 3.1$ ms, $\Delta T_E = 2.8$ ms, $T_{I,1} = 250.4$ ms, $\Delta T_I = 475.7$ ms, flip angle (FA) = 5° , slab-selective excitation with a single slab, 9 echoes, 19 inversion time points, nonselective adiabatic inversion, resolution = $1 \times 1 \times 1$ mm, matrix size = $256 \times 256 \times 160$, bandwidth (BW) = 340 Hz/px, base resolution = 256, 8 spokes, and turbo factor = 16 (i.e., 16 partitions were acquired in each repetition). The parameters were selected carefully to adequately sample the TI and TE curve, with a primary focus on generating a steady-state magnetization featuring a strong CSF signal. This is particularly important for accurate water content estimation, as CSF serves as the normalization reference for 100% water content.^{10,11} The data were undersampled along the z-dimension with a factor of 2 and 32 reference lines, resulting in a total scan time of $T_A = 7 : 15$ min and a total acceleration factor of 53.33.

To serve as a C_W reference, a VFA protocol was used, consisting of a M_0 -weighted and a T_1 -weighted 2D gradient-echo sequence (SIEMENS GRE2D).^{10,11} The sequence parameters were as follows: $T_R = 1800/818$ ms, $T_{E,1} = 5.9$ ms, $T_{E,2} = 10.0$ ms, $\Delta T_E = 2.7$ ms, 10/1 echoes, bipolar readout, FA = $40^\circ/70^\circ$, resolution = $1 \times 1 \times 1.5$ mm, matrix size = $256 \times 256 \times 90$, slice gap = 0%, slice interleaving with two slice concatenations, BW = 210 Hz/px, GRAPPA = 2 with 24 reference lines, phase partial Fourier = 6/8, and $T_A = 6 : 34/3 : 04$ min.

To serve as a T_1 reference, the T_1 mapping with partial inversion recovery (TAPIR) sequence was used.^{40,41} The sequence parameters were as follows: $T_{I,1} = 20$ ms, $\Delta T_I = 591$ ms, $T_E = 4.3$ ms, $\tau = 2400$ ms, 20 inversion time points, FA = 5° , resolution = $1 \times 1 \times 2$ mm, matrix size = $256 \times 256 \times 64$, slice gap = 25%, BW = 444 Hz/px, GRAPPA = 2 with 24 reference lines, phase partial Fourier = 6/8, and $T_A = 25 : 30$ min. The combination of a long ΔT_I and a low FA resulted in nearly undisturbed relaxation for T_1 values up to 2000 ms, significantly reducing the susceptibility of T_1 estimates to errors in the transmit field correction, bringing it more in line to the IR-spin echo-EPI sequence for T_1 validation at 7T.

However, the slice-interleaved acquisition of the TAPIR sequence allows for greater volume coverage, leading to a more accurate comparison.

A 3D MEGE sequence (SIEMENS GRE3D) was used as T_2^* and χ reference. The sequence parameters were as follows: $T_R = 45.0$ ms, $T_{E,1} = 5.22$ ms, $\Delta T_E = 2.7$ ms, FA = 5° , 12 echoes, bipolar readout, elliptical scanning, resolution = $1 \times 1 \times 1$ mm, matrix size = $256 \times 256 \times 160$, BW = 340 Hz/px, GRAPPA = 2 with 24 reference lines, phase partial Fourier = 6/8, FlowComp: Slice/Read, and $T_A = 11 : 06$ min.

An MP2RAGE sequence (SIEMENS MP2RAGE) was used for structural data and segmentation but also provided a T_1 map.³⁹ The sequence parameters were as follows: $T_R = 4300.0$ ms, $T_E = 3.0$ ms, $T_{I,1} = 840.0$ ms, $T_{I,2} = 2370.0$ ms, FA = 5° , nonselective adiabatic inversion, resolution = $1 \times 1 \times 1$ mm, matrix size = $256 \times 256 \times 160$, BW = 340 Hz/px, GRAPPA = 2 with 24 reference lines, slice partial Fourier = 6/8, turbo factor = 160, and $T_A = 9 : 59$ min.

Additionally, the transmit field inhomogeneity was mapped using a presaturated Turbo FLASH sequence (SIEMENS B1MAP TRA).⁴² The sequence parameters were as follows: $T_R = 5000$ ms, $T_E = 1.7$ ms, FA = 90° , resolution = $4 \times 4 \times 4$ mm, matrix size = $64 \times 64 \times 32$, slice gap = 25%, interleaved acquisition, BW = 490 Hz/px, GRAPPA = 2 with 16 reference lines, and $T_A = 0 : 11$ min.

3.2 | Simulations

Numerical validations were conducted using parameter maps generated based on an anatomical model of the normal brain, assuming typical values for the equilibrium longitudinal magnetization M_0 , longitudinal relaxation time T_1 , and effective transverse relaxation time T_2^* .⁴³ To simulate tissue contrast in the field map, the magnetic susceptibility was assigned according to Marques et al.⁴⁴ Before simulation, the field map underwent second-order shimming. Contrast images were generated by inserting the parameter maps in Eq. (1). A homogeneous inversion efficiency of 0.9 and an RF pulse of 5° were used without considering transmit field inhomogeneity. The remaining parameters were consistent with the ME-MPnRAGE protocol described previously.

After reconstructing the individual contrasts, the parameter maps were estimated using a four-parameter fit of the model in Eq. (1) using only a single compartment (i.e., $N_Q = 1$). This estimation was performed using a custom variable projection-based approach and a standard trust-region reflective algorithm applied to the reconstructed images.^{45,46} The parameters considered

in the fit were the real and imaginary part of M_∞ , as well as R_1^* , R_2^* , and ω . To improve stability, constraints were applied to R_1^* , R_2^* and ω , with their respective ranges set to $[1/5000 \text{ ms}, 1 \text{ ms}]$, $[1/500 \text{ ms}, 1 \text{ ms}]$, and $[-\pi/\Delta T_E, +\pi/\Delta T_E]$, respectively.

In the next step, the water content and the longitudinal relaxation time were estimated according to Eqs. (2a) and (2b), and the magnetic susceptibility was computed via dipole inversion of the field map using the open-source code provided.⁴⁷ Reference maps were generated by applying the aforementioned steps to the simulated contrast images.

To demonstrate the accuracy of the estimated parameter maps, the voxel-wise absolute difference was computed between the estimated parameter maps and the reference maps. Mean values of gray and white matter were estimated for each quantitative parameter. To analyze the effect of the regularization terms, an ablation experiment comprising the same analysis described previously was performed with data reconstructed using only the wavelet term (W), the wavelet and Casorati terms (W + C), and the wavelet and Hankel terms (W + H), with the QRAGE reconstruction comprising all three regularization terms (W + H + C). Furthermore, to analyze the method's robustness against noise, the same analysis described previously was performed again using simulated k-space data \mathbf{d} corrupted by different amounts of additive Gaussian-distributed white noise \mathbf{n} . The noise level was set such that $20 \log(\|\mathbf{d}\|/\|\mathbf{n}\|)$ equals 20 dB and 10 dB for a high and low SNR case, respectively.

3.3 | Experimental validations

As jointly reconstructing all partitions and contrasts would result in an excessively large reconstruction problem, a multistep process was used to transform the reconstruction problem into a slice-by-slice approach. First, GRAPPA was applied individually to each spoke to fill in the missing data.⁴⁸ Subsequently, the data underwent Fourier transformation along the z-direction, enabling further processing on a slice-by-slice basis. A geometric coil compression technique was then used to compress the data into eight virtual channels.⁴⁹ Gradient-delay correction was performed using the RING method.⁵⁰ Coil sensitivities were estimated through SAKE reconstruction of a calibration area, followed by ESPIRiT, using independent channel signals from the last inversion time point and the first echo.^{51,52} Finally, the MIRAGE2 algorithm was used to reconstruct the data.

After reconstruction, parameter maps were estimated using the previously described approach. It should be noted that although certain regions, such as blood vessels

and areas affected by strong static field inhomogeneity, deviated from the model, it was chosen for simplicity and comparability purposes.

Further postprocessing steps involved estimating the quantitative susceptibility map based on the field map⁴⁷ and estimating the water content map from the equilibrium longitudinal magnetization, which involves correcting for residual nonuniformity and calibrating to a region with 100% water content.¹⁰

The reference maps were estimated from the VFA, TAPIR, GRE3D, and MP2RAGE data according to Refs. 10,11,39–41,47, and 53. For the TAPIR, MP2RAGE, and QRAGE data, a homogeneous inversion efficiency of 0.75, 0.9, and 0.9 was assumed, respectively, which was based on inversion efficiency measurements and literature values,⁵⁴ and transmit field correction was performed using the acquired B_1^+ map.

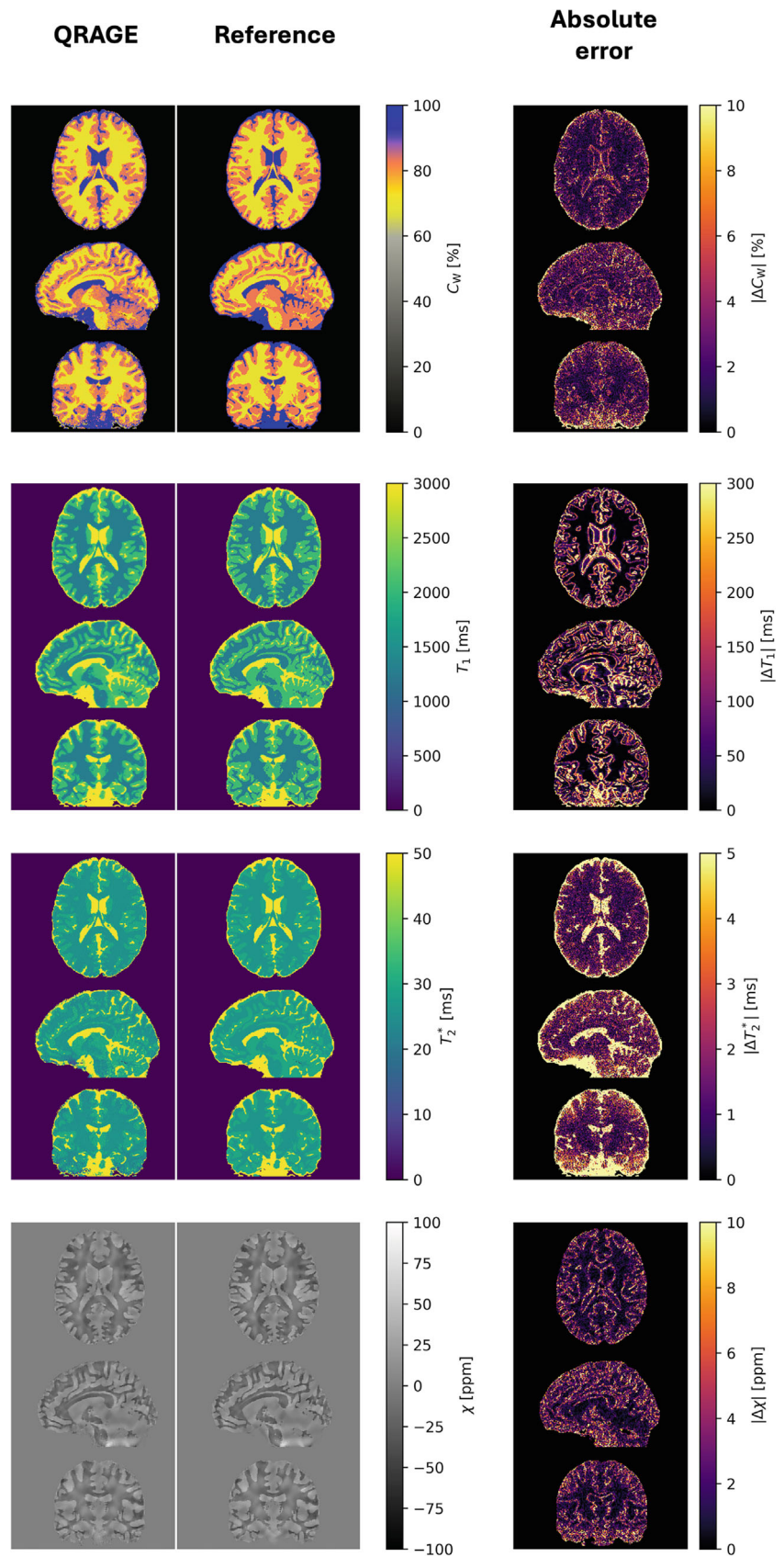
The validation of T_1 values estimated by QRAGE was performed using a so-called “revolver phantom,” which consisted of 12 tubes with varying agarose concentrations doped with NiCl to modify T_1 and T_2^* properties. The estimated T_1 parameter maps from the central slices were compared with a TAPIR reference scan. The accuracy and precision of the method were analyzed by computing the mean value of each tube from the undersampled data and comparing it with the TAPIR reference scan. Additionally, the Pearson product-moment correlation coefficient was calculated for the mean values of all tubes.

After approval of the study by the local ethics committee, MR data were acquired from 4 healthy male volunteers (aged 28 ± 2) following prior written informed consent. The subjects were scanned on 3 different days using the QRAGE method, and a single set of reference maps was also obtained. An MP2RAGE-like contrast was generated from the QRAGE data set, as follows:

$$UNI_{QRAGE}(\mathbf{r}) = \frac{\text{real}(\bar{x}_{1,1}(\mathbf{r})x_{2,1}(\mathbf{r}))}{|x_{1,1}(\mathbf{r})|^2 + |x_{2,1}(\mathbf{r})|^2} \quad (10)$$

where $x_{1,1}$ and $x_{2,1}$ are the synthetic contrast images that were generated from inserting the fitted parameters M_∞ , R_1^* , R_2^* , and ω into Eq. (1) and setting $T_{1,1} = 1000 \text{ ms}$, $T_{1,2} = 3500 \text{ ms}$, and $T_{E,1} = 0 \text{ ms}$ to match the MP2RAGE contrast.³⁹ Subsequently, tissue class maps were generated from these MP2RAGE-like contrast images using SPM.⁵⁵ To avoid interpolation and rescaling errors, additional tissue class maps were generated from the M_0 map obtained from each method for the C_W and T_1 reference methods. Similarly, tissue class maps were generated from the conventional MP2RAGE scan for the T_2^* and QSM reference methods. Mean values for C_W , T_1 , and T_2^* were computed for gray and white matter for all subjects, all three QRAGE repetitions, and the reference and MP2RAGE

FIGURE 3 The reference and estimated parameter values obtained from the simulated data sets, along with the absolute difference between them. The parameters include C_w , T_1 , T_2^* , and χ , and the analysis is performed without the addition of any noise. QRAGE, quantitative rapid gradient echo.



scans individually. In the case of the C_w and T_1 reference methods, the lower 30 and 26 brain slices, respectively, were excluded from the comparison due to poor transmit

field homogeneity and low inversion efficiency. To analyze the effect of the regularization terms, an ablation experiment was performed in which data from all subjects

TABLE 1 Mean values of quantitative parameters for simulated data reconstructed using different regularization terms.

		Method	Mean	SD	Reference	Difference
C_W [%]	GM	W	83.4	5.1		0.4
		W + C	84.1	3.7		1.1
		W + H	83.2	2.2	83.0 (0.0)	0.2
		W + H + C	83.3	2.0		0.3
	WM	W	70.0	2.9		0.0
		W + C	70.8	2.3		0.8
		W + H	70.1	1.8	70.0 (0.0)	0.1
		W + H + C	70.2	1.6		0.2
T_1 [ms]	GM	W	2092	131		27
		W + C	2079	94		14
		W + H	2063	65	2065 (0)	-2
		W + H + C	2063	20		-2
	WM	W	1314	68		30
		W + C	1304	41		20
		W + H	1281	42	1284 (0)	-3
		W + H + C	1285	8		1
T_2^* [ms]	GM	W	28.2	5.8		-1.8
		W + C	28.4	4.6		-1.6
		W + H	29.4	1.7	30.0 (0.0)	-0.6
		W + H + C	29.3	1.8		-0.7
	WM	W	25.2	2.7		-0.8
		W + C	25.4	2.1		-0.6
		W + H	25.6	1.2	26.0 (0.0)	-0.4
		W + H + C	25.6	1.2		-0.4
χ [ppb]	GM	W	23.1	23.6		-7.7
		W + C	27.5	24.6		-3.3
		W + H	30.3	25.8	30.8 (25.8)	-0.5
		W + H + C	30.3	25.8		-0.5
	WM	W	-18.7	22.5		+4.1
		W + C	-21.5	25.7		+1.3
		W + H	-22.7	28.2	-22.8 (28.4)	+0.1
		W + H + C	-22.7	28.1		+0.1

Bold values indicate the lowest value, i.e., best method, for a certain parameter, e.g., C_W , and tissue type, e.g., GM.

Abbreviations: C, Casorati term; GM, gray matter; H, Hankel term; W, Wavelet term; WM, white matter.

acquired in the first repetition were further reconstructed using only the wavelet term (W), the wavelet and Casorati terms (W + C), and the wavelet and Hankel terms (W + H), with the QRAGE reconstruction comprising all three regularization terms (W + H + C).

3.4 | Reconstruction

The reconstruction process was conducted offline using a custom *Python* software package developed in-house. Data preprocessing and postprocessing were carried out on the

TABLE 2 Mean values of T_1 for phantom data.

Tube	T_1 [ms]		Rel. error
	TAPIR	QRAGE	
1	890	856	3.89%
2	905	864	4.47%
3	1189	1112	6.50%
4	1302	1242	4.65%
5	1342	1339	0.21%
6	1346	1380	2.52%
7	1501	1454	3.17%
8	1607	1620	0.80%
9	1649	1632	1.05%
10	1664	1691	1.63%
11	1765	1756	0.47%
12	1911	1912	0.03%

Abbreviation: QRAGE, quantitative rapid gradient echo; TAPIR, T_1 mapping with partial inversion recovery.

institute compute cluster, whereas the JURECA system at the Jülich Supercomputing Center enabled parallel reconstruction of all slices.⁵⁶ The entire reconstruction process took approximately 6 h.

In the numerical, phantom, and in vivo experiments, the reconstruction was performed with five inner iterations (conjugate gradient algorithm on the normal equation) and 250 outer iterations (alternating direction method of multipliers). For the wavelet operator, D4 wavelets were used, and a 5×5 neighborhood was used for the Casorati operator. The regularization parameters were set as $\lambda_W = 0.001$, $\lambda_H = 0.1$, and $\lambda_C = 0.01$.

4 | RESULTS

4.1 | Simulations

Figure 3 shows the reference and estimated parameter maps of C_W , T_1 , T_2^* , and χ obtained from the simulated data, along with the absolute difference. The reference and estimated parameter maps exhibit excellent visual agreement. Among these parameters, T_2^* demonstrates the highest sensitivity and is the only one displaying systematic errors, which can be seen in the absolute difference maps. These errors are closely related to the inhomogeneity of the static magnetic field, which leads to an underestimation of T_2^* . This can be further seen in Figure S2, where the parameter maps obtained from data reconstructed using different regularization terms are shown alongside a field map of $\Delta\omega_0$. It can be observed that the inclusion of the

Hankel term significantly reduces the overall error and the susceptibility to $\Delta\omega_0$ inhomogeneity, which is otherwise present, particularly in C_W and T_2^* . The estimated parameter maps with added noise (low and high SNR) also show good agreement with the reference maps and can be found in Figure S3. Higher noise levels in the k-space data lead to random noise in the parameter maps without introducing systematic errors, particularly in areas affected by strong $\Delta\omega_0$ inhomogeneity.

Table 1 provides the mean values of all four parameters for gray and white matter estimated from data reconstructed using different regularization terms. For QRAGE, the absolute differences from the reference values are 0.3% or below for C_W , below 2 ms for T_1 , below 0.7 ms for T_2^* , and below 0.6 ppb for χ . It can be seen that the inclusion of the Hankel term produces the lowest differences to the reference values. With the exception of T_2^* in gray matter, the further addition of the Casorati term leads to lower SDs in the parameter maps, particularly in T_1 , but in a few cases results in increased differences to the reference values of 0.1% in C_W and 0.1 ms in T_2^* . Table S1 displays the mean values of all four parameters for gray and white matter from data with different levels of added noise. Remarkably, for moderate levels of noise, the mean values remain unchanged, and even with the introduction of high levels of noise, the mean values change only slightly, highlighting the exceptional robustness of the method. In particular, C_W changed less than 0.1%, T_1 less than 2 ms, T_2^* less than 0.3 ms, and χ less than 0.1 ppb with increasing levels of noise.

4.2 | Phantom and in vivo experiments

The phantom experiments demonstrated excellent agreement between the TAPIR reference data and the QRAGE sequence across a broad range of clinically relevant T_1 values (1000–2000 ms), encompassing typical values for both gray matter and white matter. This is underlined by a high correlation coefficient of 0.996 between the mean T_1 values of the TAPIR and QRAGE measurement. Mean T_1 values for each tube estimated by the TAPIR and QRAGE method as well as the relative error for the QRAGE method can be found in Table 2, and the correlation plot and T_1 parameter maps of both methods can be found in Figure S4, where good visual agreement between the QRAGE and TAPIR map can be observed. Figure S5 shows the contrast images of the first five TI points and the first three TE points from the in vivo measurements of a healthy representative volunteer, and Figure 4 illustrates the estimated parameter maps derived from these contrast images, including C_W , T_1 , T_2^* , and χ of the first repetition of the QRAGE method and the reference methods. To assess accuracy and

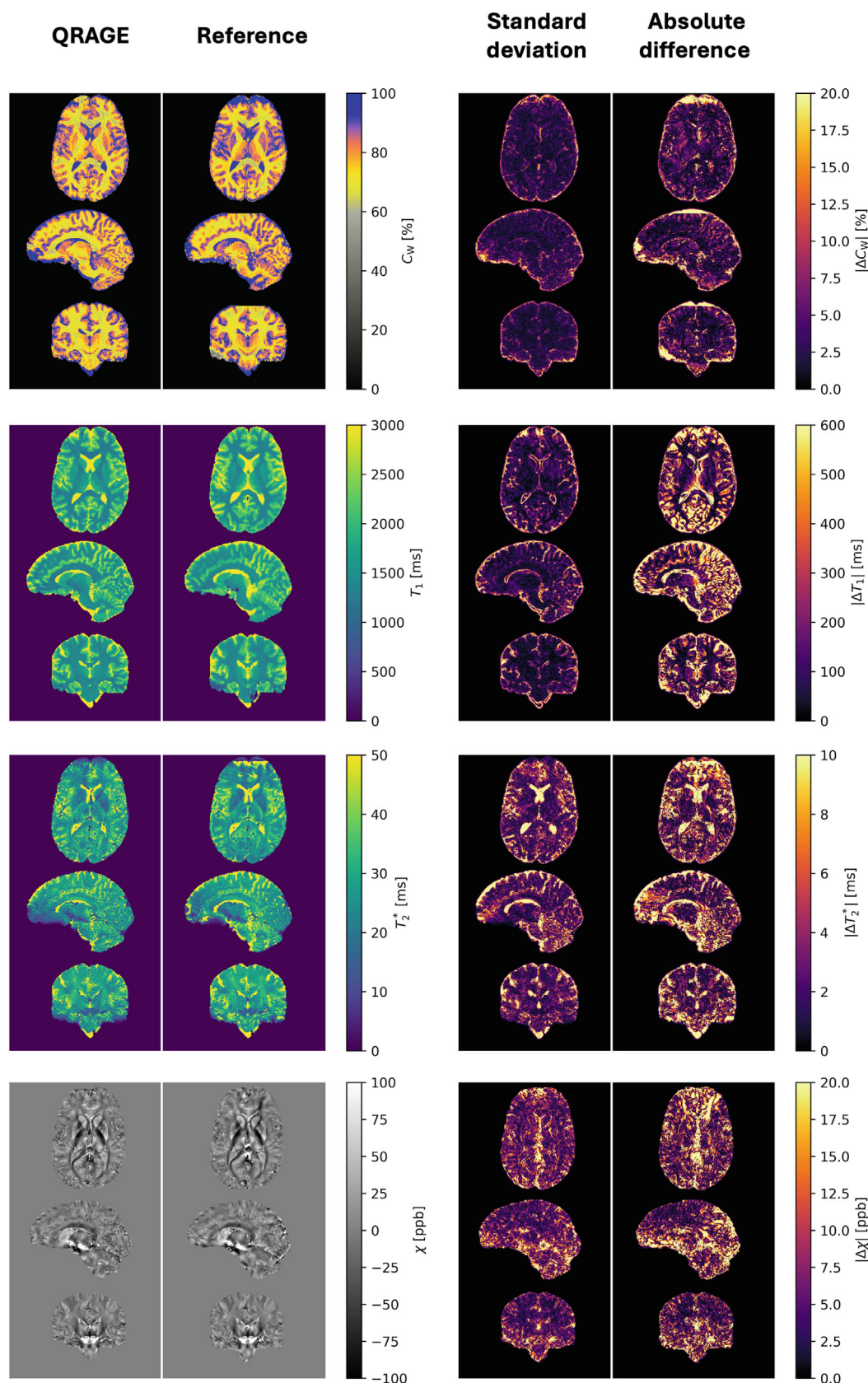
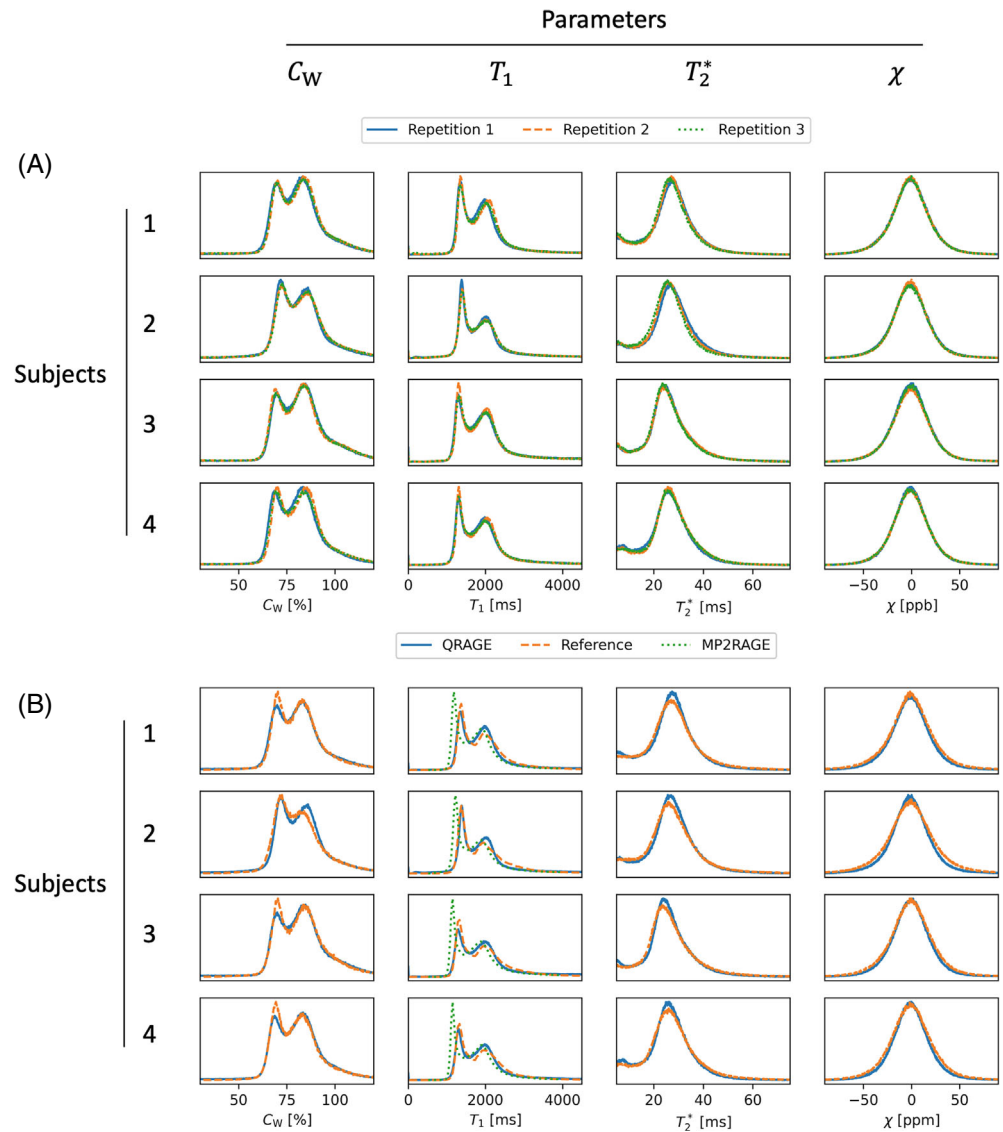


FIGURE 4 Estimated parameter maps derived from the in vivo data sets of a representative healthy volunteer. The parameter maps include C_w , T_1 , T_2^* , and χ for the first repetition of the quantitative rapid gradient-echo (QRAGE) method as well as the reference methods. Also shown are the voxel-wise SD across repetitions of the QRAGE method and the voxel-wise absolute difference of the voxel-wise mean of the QRAGE method across repetitions to the reference methods.

FIGURE 5 (A)

Histogram analysis of the test–retest experiments, showcasing the overlay of histograms for water content, T_1 , T_2^* , and χ derived from three different repetitions of quantitative rapid gradient-echo (QRAGE) of all volunteers. (B) Test-reference experiments, displaying the overlay of the averaged histogram for water content, T_1 , T_2^* , and χ over the repetitions of QRAGE of all volunteers, along with the histogram of the reference methods.



test–retest stability, maps of the SD of the QRAGE method across repetitions and the absolute difference of the mean of the QRAGE method across repetitions to the reference method are shown for each parameter. The parameter maps exhibit favorable visual agreement between QRAGE and the reference methods, as well as consistency between repetitions of the QRAGE method. The parameter maps obtained from data of the same volunteer reconstructed using different regularization terms are shown in Figure S6 alongside a field map of $\Delta\omega_0$. Again, it can be observed that the inclusion of the Hankel term significantly reduces the susceptibility to $\Delta\omega_0$ inhomogeneity, in particular in the C_w and T_2^* maps, and that the further inclusion of the Casorati term reduces overall noise, in particular in the T_1 map, which is in agreement with the simulation results.

The accuracy and precision of the QRAGE method were further validated through histogram analysis in both the test–retest and test-reference analyses, which are shown in Figure 5 for all volunteers. In the test–retest

analysis, the histograms demonstrate excellent agreement between repetitions for all subjects, confirming the robustness of the QRAGE method. Although the test-reference analysis also reveals good agreement between QRAGE and the reference methods, slight deviations in the shape of the histograms are observed. These deviations partly arise from differences in resolution between the QRAGE and reference methods, particularly in the case of C_w and T_1 .

The accuracy and precision are further validated via Bland–Altman-like analysis, comparing the mean values for gray and white matter of all parameters estimated by QRAGE to the values provided by the reference methods, thereby investigating the effect of different regularization terms and analyzing test–retest stability as shown in Figure 6. The results agree with the simulation results, showing that, in particular, the Hankel term improves the accuracy and precision of all estimated parameters, with the exception of C_w , where it leads to a small

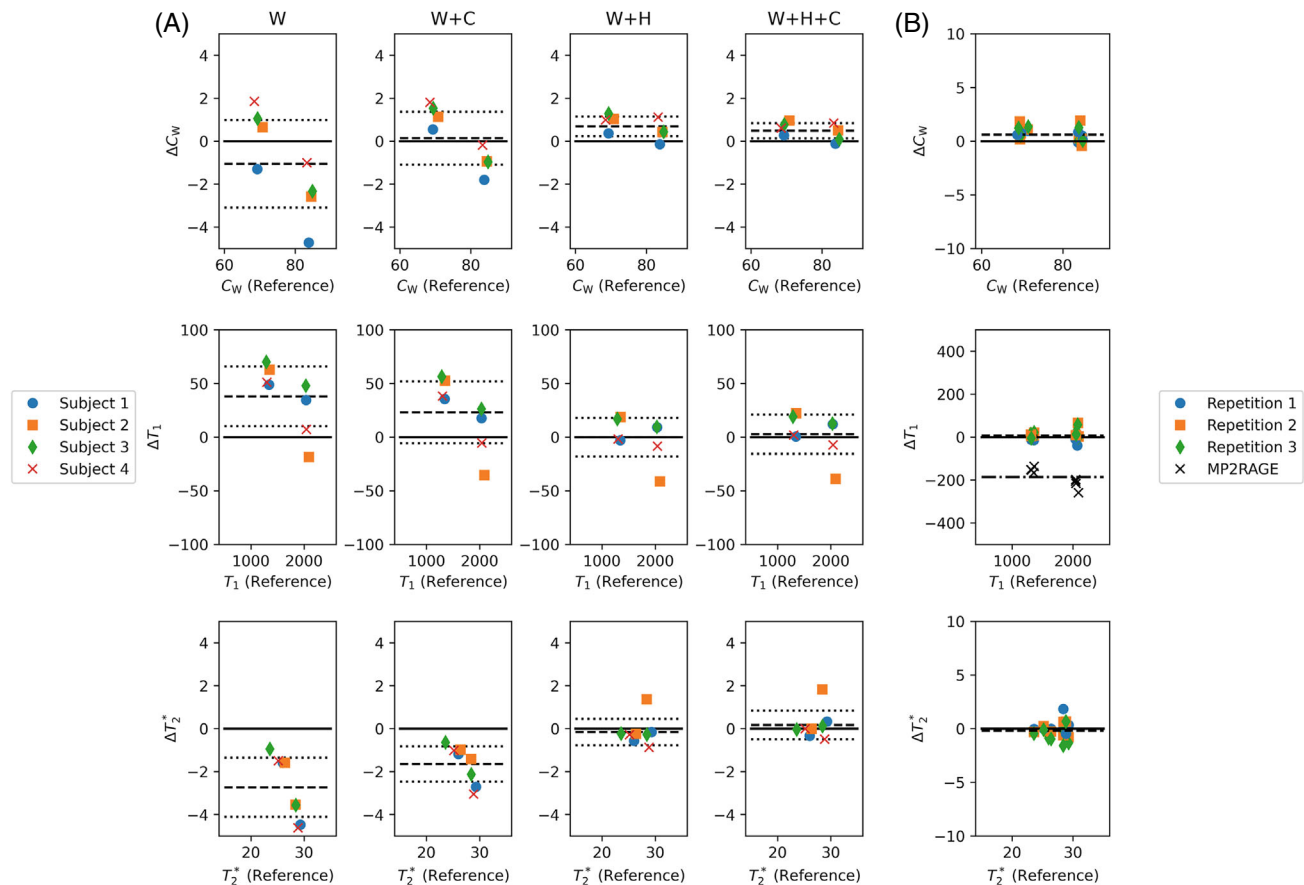


FIGURE 6 (A) Bland–Altman-like diagram showing the mean values of water content, T_1 , and T_2^* for gray matter and white matter of all subjects using data of the first repetition reconstructed using different regularization terms compared with the reference methods. (B) Bland–Altman-like diagram showing the mean values of water content, T_1 , and T_2^* for gray matter and white matter of the quantitative rapid gradient-echo (QRAGE) method of all repetitions compared with the reference methods. C, Casorati term; H, Hankel term; W, Wavelet term.

overestimation of about 0.6%. It also shows that while QRAGE is in good agreement with TAPIR, T_1 estimated from MP2RAGE shows a systematic underestimation of about 200–300 ms.

Table 3 presents the mean values for all four quantitative parameters, averaged over gray and white matter for all subjects. QRAGE exhibits exceptional precision, as evidenced by low SDs between repetitions, which are, on average, 0.3% or below for C_W , 17 ms or below for T_1 , and 0.7 ms or below for T_2^* for all subjects. Moreover, QRAGE demonstrates high accuracy by displaying good agreement with the reference methods. The differences in C_W are, on average, 0.8% or below, in T_1 are 11 ms or below, and in T_2^* are 0.3 ms or below for all subjects. These differences fall within the range of QRAGE's precision, align well with the simulation results, and agree well with the values from literature for water content mapping at 3 T and T_1 mapping at 7 T, further affirming the method's reliability.^{10,24}

Finally, the QRAGE method also generates an MP2RAGE-like contrast (Figure 7), which was used here for tissue mask segmentation using *SPM*. Visually, the

contrast obtained from QRAGE is comparable to the contrast produced by a reference MP2RAGE scan acquired within this study.

5 | DISCUSSION

In this study, we present a novel technique called QRAGE, which enables fast and robust multiparametric qMRI at UHF, thereby potentially opening up a wide range of clinical MR applications. The acquisition time of QRAGE is 7 min and 15 s, during which it generates parametric maps with 1-mm³ isotropic resolution and full brain coverage. Through numerical simulations, phantom experiments, and in vivo studies, we have demonstrated the accurate and precise estimation of various quantitative MRI parameters, including water content, T_1 , T_2^* , and magnetic susceptibility. Notably, the acquisition time of QRAGE is comparable to that of a qualitative MP2RAGE scan, while providing similar image contrast. This feature positions QRAGE as a potential drop-in replacement for

TABLE 3 Mean values of quantitative parameters for in vivo data.

		Subject	QRAGE mean (SD)	MP2RAGE	Reference	Difference QRAGE reference	Difference MP2RAGE reference
C_w [%]	GM	1	83.9 (0.2)		83.8	0.1	
		2	84.8 (0.1)		84.5	0.3	
		3	84.8 (0.2)		84.9	−0.1	
		4	84.7 (0.4)		83.3	1.4	
		Mean	84.6 (0.2)		84.1	0.4	
	WM	1	69.8 (0.2)		69.3	0.5	
		2	71.9 (0.2)		70.8	1.1	
		3	69.9 (0.2)		69.4	0.5	
		4	69.7 (0.5)		68.5	1.2	
		Mean	70.3 (0.3)		69.5	0.8	
T_1 [ms]	GM	1	2089 (29)	1832	2048	41	−216
		2	2077 (19)	1831	2090	−13	−259
		3	2055 (11)	1837	2043	12	−206
		4	2049 (10)	1847	2045	4	−198
		Mean	2068 (17)	1837	2068	11	−220
	WM	1	1353 (9)	1191	1357	−4	−166
		2	1379 (5)	1225	1361	+18	−136
		3	1317 (6)	1157	1309	8	−152
		4	1312 (7)	1162	1316	−4	−155
		Mean	1340 (7)	1184	1340	−5	−152
T_2^* [ms]	GM	1	28.7 (0.7)		29.3	−0.6	
		2	28.3 (1.4)		28.4	−0.1	
		3	28.6 (0.3)		28.4	0.2	
		4	29.1 (0.5)		28.8	0.3	
		Mean	28.7 (0.7)		28.7	0.0	
	WM	1	25.5 (0.3)		26.0	−0.5	
		2	26.0 (0.4)		26.4	−0.4	
		3	23.3 (0.2)		23.6	−0.3	
		4	25.2 (0.1)		25.2	0.0	
		Mean	25.0 (0.3)		25.3	−0.3	

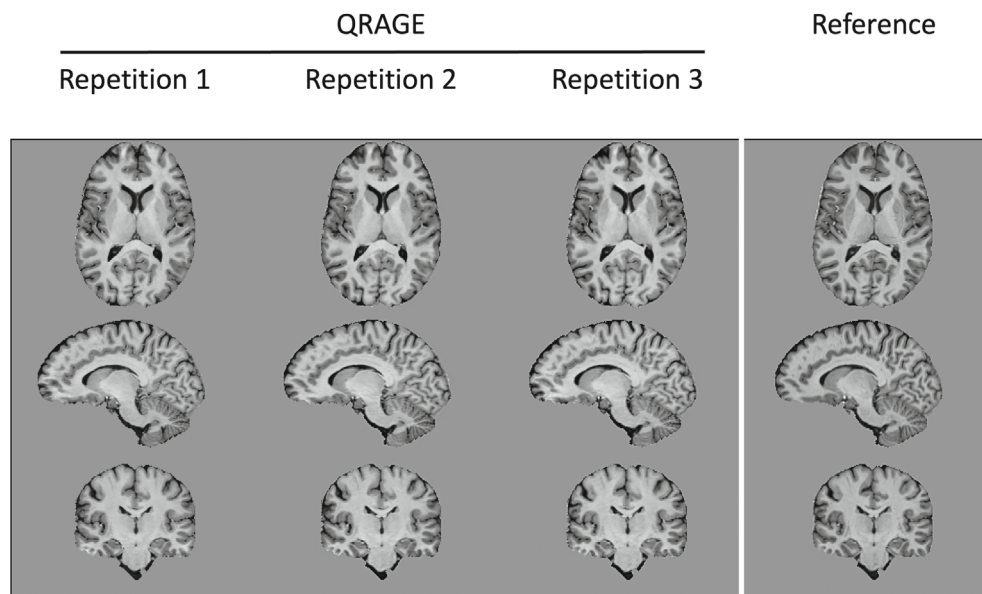
Note: QRAGE values are given as mean and SD over repetitions.

Abbreviations: GM, gray matter; QRAGE, quantitative rapid gradient echo; WM, white matter.

the widely used MP2RAGE sequence in neuroscientific research protocols if the long reconstruction times can be overcome in due course. Assuming this, it is likely that QRAGE will find a high acceptance rate among researchers.

Although the ME-MP2RAGE sequence can yield high-quality T_2^* and magnetic susceptibility maps, it tends to underestimate T_1 .^{13,24} VFA-based methods also face challenges in providing accurate T_1 estimates, particularly

in the presence of high transmit field inhomogeneity at UHF. Conversely, Look-Locker-based methods such as TAPIR and MPnRAGE, as well as QRAGE with their extensive inversion time sampling, demonstrate robustness in accurately estimating T_1 values.^{39–41,57} Because T_1 is an essential correction factor in water content mapping, QRAGE is better suited for applications at UHF compared with the well-established VFA method at 3 T.

**FIGURE 7**

MP2RAGE-like contrast generated by quantitative rapid gradient-echo (QRAGE) for a representative volunteer, showcasing the images obtained for each of the measured repetitions. Additionally, the uniform images (UNI) image provided by the MP2RAGE reference measurement is included for comparison.

To achieve an acceptable measurement time despite the high number of inversion time points, QRAGE relies on a high acceleration factor, which places pressure on the reconstruction algorithm. In this study, we presented the MIRAGE2 algorithm, which solves a convex problem and guarantees convergence to a globally optimal solution. MIRAGE2 accounts for multi-exponential behavior and exhibits robustness against partial volume artifacts, noise, and static magnetic field inhomogeneity. As a future application, conducting 2D multi-exponential relaxometry would provide insights into whether a better identification of myelin water, which exhibits significantly shorter T_1 and T_2^* values compared with extracellular white matter, is achievable.^{58,59} A potential challenge could be that our model may be oversimplified, as it does not account for additional effects such as chemical exchange between water pools.

One of the fundamental challenges of the QRAGE method lies in the substantial computing power requirements and its lengthy reconstruction time, making it unsuitable for applications in which low latencies are crucial. However, the fundamental reconstruction problem is inherently parallel, and further parallelization of our code would not only allow one to speed up the reconstruction but also would enable the simultaneous reconstruction of all slices. Enabling such capability would allow the use of a koosh ball-like sampling scheme similar to the one used in the MPnRAGE sequence.¹³ This sampling scheme permits higher acceleration factors along the z-dimension, potentially reducing acquisition time further. Although radial sampling already provides a degree of motion robustness, koosh ball-like sampling additionally offers the potential for self-navigated motion correction, thereby further minimizing sensitivity to patient

motion and potential image artifacts.⁶⁰ Additionally, the MIRAGE2 algorithm could potentially benefit from incorporating a deep learning-based spatial denoiser, replacing the stationary wavelet transform, thus forming a hybrid architecture. Previous studies using hybrid architectures, such as the model-based deep learning reconstruction technique, have demonstrated improved results compared with wavelet-based compressed-sensing MRI.⁶¹

ACKNOWLEDGMENTS

The authors thank Michael Schöneck and Annette Mock for their valuable assistance in constructing the phantom as well as Soheli Herff for his valuable support in harnessing the power of the Jülich supercomputer. Thanks are also due to Claire Rick for proofreading the manuscript. The authors gratefully acknowledge the computing time granted through JARA on the supercomputer JURECA at Forschungszentrum Jülich. Additionally, they express their appreciation for the HPC support provided through the EuroCC project. Open Access funding enabled and organized by Projekt DEAL.

ORCID

Markus Zimmermann  <https://orcid.org/0000-0003-1273-5218>

Zaheer Abbas  <https://orcid.org/0000-0002-0650-8388>

Yannic Sommer  <https://orcid.org/0009-0005-5139-4040>

Alexander Lewin  <https://orcid.org/0009-0004-5371-0644>

Shukti Ramkiran  <https://orcid.org/0000-0001-8253-1873>

Jörg Felder  <https://orcid.org/0000-0001-6431-4322>

Wieland A. Worthoff  <https://orcid.org/0000-0001-9121-8790>

Ana-Maria Oros-Peusquens  <https://orcid.org/0000-0003-1869-3354>

Seong Dae Yun  <https://orcid.org/0000-0001-7398-1899>

N. Jon Shah  <https://orcid.org/0000-0002-8151-6169>

REFERENCES

- Weiskopf N, Edwards LJ, Helms G, Mohammadi S, Kirilina E. Quantitative magnetic resonance imaging of brain anatomy and in vivo histology. *Nat Rev Phys*. 2021;3:570-588.
- Caan MWA, Bazin PL, Marques JP, de Hollander G, Dumoulin SO, van der Zwaag W. MP2RAGEME: T_1 , T_2^* , and QSM mapping in one sequence at 7 Tesla. *Hum Brain Mapp*. 2019;40:1786-1798.
- Oros-Peusquens A-M, Loução R, Abbas Z, Gras V, Zimmermann M, Shah NJ. A single-scan, rapid whole-brain protocol for quantitative water content mapping with neurobiological implications. *Front Neurol*. 2019;10:1333.
- Vargas MI, Martelli P, Xin L, et al. Clinical neuroimaging using 7 T MRI: challenges and prospects. *J Neuroimaging*. 2018;28:5-13.
- Stüber C, Morawski M, Schäfer A, et al. Myelin and iron concentration in the human brain: a quantitative study of MRI contrast. *Neuroimage*. 2014;93:95-106.
- Harkins KD, Xu J, Dula AN, et al. The microstructural correlates of T_1 in white matter. *Magn Reson Med*. 2016;75:1341-1345.
- Deistung A, Schäfer A, Schweser F, et al. High-resolution MR imaging of the human brainstem in vivo at 7 Tesla. *Front Hum Neurosci*. 2013;7:710.
- Mezer A, Rokem A, Berman S, Hastie T, Wandell BA. Evaluating quantitative proton-density-mapping methods: proton-density mapping. *Hum Brain Mapp*. 2016;37:3623-3635.
- Neeb H, Ermer V, Stöcker T, Shah NJ. Fast quantitative mapping of absolute water content with full brain coverage. *Neuroimage*. 2008;42:1094-1109.
- Abbas Z, Gras V, Möllenhoff K, Keil F, Oros-Peusquens AM, Shah NJ. Analysis of proton-density bias corrections based on T_1 measurement for robust quantification of water content in the brain at 3 tesla. *Magn Reson Med*. 2014;72:1735-1745.
- Abbas Z, Gras V, Möllenhoff K, Oros-Peusquens A-M, Shah NJ. Quantitative water content mapping at clinically relevant field strengths: a comparative study at 1.5T and 3T. *Neuroimage*. 2015;106:404-413.
- Schall M, Zimmermann M, Iordanishvili E, Gu Y, Shah NJ, Oros-Peusquens AM. A 3D two-point method for whole-brain water content and relaxation time mapping: comparison with gold standard methods. *PLoS One*. 2018;13:e0201013.
- Kecskemeti S, Samsonov A, Hurley SA, Dean DC, Field A, Alexander AL. MPnRAGE: a technique to simultaneously acquire hundreds of differently contrasted MPRAGE images with applications to quantitative T_1 mapping: MPnRAGE T_1 imaging. *Magn Reson Med*. 2016;75:1040-1053.
- Ma D, Gulani V, Seiberlich N, et al. Magnetic resonance fingerprinting. *Nature*. 2013;495:187-192.
- Wang F, Dong Z, Reese TG, et al. Echo planar time-resolved imaging (EPTI). *Magn Reson Med*. 2019;81:3599-3615.
- Wang F, Dong Z, Reese TG, Rosen B, Wald LL, Setsompop K. 3D Echo planar time-resolved imaging (3D-EPTI) for ultrafast multi-parametric quantitative MRI. *Neuroimage*. 2022;250:118963.
- Fujita S, Hagiwara A, Hori M, et al. Three-dimensional high-resolution simultaneous quantitative mapping of the whole brain with 3D-QALAS: an accuracy and repeatability study. *Magn Reson Imaging*. 2019;63:235-243.
- Jun Y, Cho J, Wang X, et al. SSL-QALAS: Self-supervised learning for rapid multiparameter estimation in quantitative MRI using 3D-QALAS. *Magn Reson Med*. 2023;90:2019-2032.
- Jiang Y, Ma D, Jerecic R, et al. MR fingerprinting using the quick echo splitting NMR imaging technique. *Magn Reson Med*. 2017;77:979-988.
- Cloos MA, Knoll F, Zhao T, et al. Multiparametric imaging with heterogeneous radiofrequency fields. *Nat Commun*. 2016;7:12445.
- Buonincontri G, Schulte RF, Cosottini M, Tosetti M. Spiral MR fingerprinting at 7T with simultaneous B_1 estimation. *Magn Reson Imaging*. 2017;41:1-6.
- Metere R, Kober T, Möller HE, Schäfer A. Simultaneous quantitative MRI mapping of T_1 , T_2^* and magnetic susceptibility with multi-Echo MP2RAGE. *PLoS One*. 2017;12:e0169265.
- Sun H, Cleary JO, Glarin R, et al. Extracting more for less: multi-echo MP2RAGE for simultaneous T_1 -weighted imaging, T_1 mapping, mapping, SWI, and QSM from a single acquisition. *Magn Reson Med*. 2020;83:1178-1191.
- Olsson H, Andersen M, Kadhim M, Helms G. MP3RAGE: simultaneous mapping of T_1 and B_1^+ in human brain at 7T. *Magn Reson Med*. 2022;87:2637-2649.
- Block KT, Uecker M, Frahm J. Model-based iterative reconstruction for radial fast spin-echo MRI. *IEEE Trans Med Imaging*. 2009;28:1759-1769.
- Zimmermann M, Abbas Z, Dzieciol K, Shah NJ. Accelerated parameter mapping of multiple-echo gradient-echo data using model-based iterative reconstruction. *IEEE Trans Med Imaging*. 2018;37:626-637.
- Tan Z, Unterberg-Buchwald C, Blumenthal M, et al. Free-breathing liver fat, R_2^* and B_0 field mapping using multi-echo radial FLASH and regularized model-based reconstruction. *IEEE Trans Med Imaging*. 2023;42:1374-1387.
- Lee GR, Griswold MA, Tkach JA. Rapid 3D radial multi-echo functional magnetic resonance imaging. *Neuroimage*. 2010;52:1428-1443.
- Zhang T, Pauly JM, Levesque IR. Accelerating parameter mapping with a locally low rank constraint. *Magn Reson Med*. 2015;73:655-661.
- Cao P, Zhu X, Tang S, Leynes A, Jakary A, Larson PEZ. Shuffled magnetization-prepared multicontrast rapid gradient-echo imaging. *Magn Reson Med*. 2018;79:62-70.
- Peng X, Ying L, Liu Y, Yuan J, Liu X, Liang D. Accelerated exponential parameterization of T_2 relaxation with model-driven low rank and sparsity priors (MORASA): accelerated T_2 mapping with MORASA. *Magn Reson Med*. 2016;76:1865-1878.
- Tran-Gia J, Wech T, Bley T, Köstler H. Model-based acceleration of look-locker T_1 mapping. *PLoS One*. 2015;10:e0122611.
- Wang X, Roeloffs V, Klosowski J, et al. Model-based T_1 mapping with sparsity constraints using single-shot inversion-recovery radial FLASH. *Magn Reson Med*. 2017;79:730-740. doi:10.1002/mrm.26726
- Wang X, Tan Z, Scholand N, Roeloffs V, Uecker M. Physics-based reconstruction methods for magnetic resonance imaging. *Philos Trans R Soc Math Phys Eng Sci*. 2021;379:20200196.

35. Haacke EM, Brown RW, Thompson MR, Venkatesan R. *Magnetic Resonance Imaging*. Wiley-Liss; 1999.
36. *Quantitative MRI of the Brain: Measuring Changes Caused by Disease*. Wiley; 2003.
37. de Rochefort L, Brown R, Prince MR, Wang Y. Quantitative MR susceptibility mapping using piece-wise constant regularized inversion of the magnetic field. *Magn Reson Med*. 2008;60:1003-1009.
38. Winkelmann S, Schaeffter T, Koehler T, Eggers H, Doessel O. An optimal radial profile order based on the golden ratio for time-resolved MRI. *IEEE Trans Med Imaging*. 2007;26:68-76.
39. Marques JP, Kober T, Krueger G, van der Zwaag W, van de Moortele PF, Gruetter R. MP2RAGE, a self bias-field corrected sequence for improved segmentation and T_1 -mapping at high field. *Neuroimage*. 2010;49:1271-1281.
40. Shah NJ, Zaitsev M, Steinhoff S, Zilles K. A new method for fast multislice T_1 mapping. *Neuroimage*. 2001;14:1175-1185.
41. Zaitsev M, Steinhoff S, Shah NJ. Error reduction and parameter optimization of the TAPIR method for fast T_1 mapping. *Magn Reson Med*. 2003;49:1121-1132.
42. Chung S, Kim D, Breton E, Axel L. Rapid B_1^+ mapping using a preconditioning RF pulse with TurboFLASH readout. *Magn Reson Med*. 2010;64:439-446.
43. Cocosco CA, Kollokian V, Kwan RKS, Pike GB, Evans AC. BrainWeb: online interface to a 3D MRI simulated brain database. *Proceedings of the 3rd International Conference on Functional Mapping of the Human Brain*. NeuroImage; 1997.
44. Marques JP, Meineke J, Milovic C, et al. QSM reconstruction challenge 2.0: a realistic in silico head phantom for MRI data simulation and evaluation of susceptibility mapping procedures. *Magn Reson Med*. 2021;86:526-542.
45. Golub G, Pereyra V. Separable nonlinear least squares: the variable projection method and its applications. *Inverse Probl*. 2003;19:R1-R26.
46. Virtanen P, Gommers R, Oliphant TE, et al. SciPy 1.0: fundamental algorithms for scientific computing in Python. *Nat Methods*. 2020;17:261-272.
47. Langkammer C, Bredies K, Poser BA, et al. Fast quantitative susceptibility mapping using 3D EPI and total generalized variation. *Neuroimage*. 2015;111:622-630.
48. Griswold MA, Jakob PM, Heidemann RM, et al. Generalized autocalibrating partially parallel acquisitions (GRAPPA). *Magn Reson Med*. 2002;47:1202-1210.
49. Zhang T, Pauly JM, Vasanawala SS, Lustig M. Coil compression for accelerated imaging with Cartesian sampling. *Magn Reson Med*. 2013;69:571-582.
50. Rosenzweig S, Holme HCM, Uecker M. Simple auto-calibrated gradient delay estimation from few spokes using radial intersections (RING). *Magn Reson Med*. 2019;81:1898-1906.
51. Shin PJ, Larson PEZ, Ohliger MA, et al. Calibrationless parallel imaging reconstruction based on structured low-rank matrix completion. *Magn Reson Med*. 2014;72:959-970.
52. Uecker M, Lai P, Murphy MJ, et al. ESPIRiT—an eigenvalue approach to autocalibrating parallel MRI: where SENSE meets GRAPPA. *Magn Reson Med*. 2014;71:990-1001.
53. Karakuzu A, Boudreau M, Duval T, et al. qMRLab: quantitative MRI analysis, under one umbrella. *J Open Source Softw*. 2020;5:2343.
54. O'Brien KR, Magill AW, Delacoste J, et al. Dielectric pads and low- B_1^+ adiabatic pulses: complementary techniques to optimize structural T_1 w whole-brain MP2RAGE scans at 7 Tesla: how to acquire whole-brain MP2RAGE at 7T. *J Magn Reson Imaging*. 2014;40:804-812.
55. Ashburner J, Friston KJ. Unified segmentation. *Neuroimage*. 2005;26:839-851.
56. Thörnig P. JURECA: data centric and booster modules implementing the modular supercomputing architecture at Jülich supercomputing Centre. *J Large-Scale Res Facil JLSRF*. 2021;7:A182.
57. Claeser R, Zimmermann M, Shah NJ. Sub-millimeter T_1 mapping of rapidly relaxing compartments with gradient delay corrected spiral TAPIR and compressed sensing at 3T. *Magn Reson Med*. 2019;82:1288-1300.
58. Deoni SCL, Rutt BK, Arun T, Pierpaoli C, Jones DK. Gleaning multicomponent T_1 and T_2 information from steady-state imaging data. *Magn Reson Med*. 2008;60:1372-1387.
59. Zimmermann M, Oros-Peusquens AM, Iordanishvili E, et al. Multi-exponential relaxometry using l_1 -regularized iterative NNLS (MERLIN) with application to myelin water fraction imaging. *IEEE Trans Med Imaging*. 2019;38:2676-2686.
60. Kecskesti S, Alexander AL. Three-dimensional motion-corrected T_1 relaxometry with MPnRAGE. *Magn Reson Med*. 2020;84:2400-2411.
61. Aggarwal HK, Mani MP, Jacob M. MoDL: model-based deep learning architecture for inverse problems. *IEEE Trans Med Imaging*. 2019;38:394-405.

SUPPORTING INFORMATION

Additional supporting information may be found in the online version of the article at the publisher's website.

Data S1 Supporting Information.

How to cite this article: Zimmermann M, Abbas Z, Sommer Y, et al. QRAGE—Simultaneous multiparametric quantitative MRI of water content, T_1 , T_2 , and magnetic susceptibility at ultrahigh field strength. *Magn Reson Med*. 2025;93:228-244. doi: 10.1002/mrm.30272